





Intelligent Reflecting Surfaces for Underwater Visible Light Communications

Yalçın Ata , Hanaa Abumarshoud, *Senior Member, IEEE*, Lina Bariah , *Senior Member, IEEE*, Sami Muhaidat , *Senior Member, IEEE*, and Muhammad Ali Imran , *Fellow, IEEE*

Abstract—Intelligent reflecting surfaces (IRSs) offer paradigm shift towards enhancing the capabilities of wireless communications. The use of this emerging technology in the realm of underwater wireless systems is a promising solution to overcome the limitations pertinent to such challenging environments. In this paper, we quantify the performance enhancement offered by the integration of IRS technology in the context of underwater optical wireless communication (OWC). Specifically, we derive a closed-form expression for the outage probability over log-normal channels, taking into consideration the underwater attenuation, pointing error, and turbulence effects. The underwater turbulent medium is characterized by the recently introduced Oceanic Turbulence Optical Power Spectrum (OTOPS) model that uses the practical values of average temperature and salinity concentration in earth basins. The presented numerical results take into account the effects of the turbulent medium as well as the communication system parameters (i.e., communication range, receiver aperture diameter, number of IRS). Our results show that IRSs can offer significant enhancement in the reliability of underwater OWC systems under attenuation, beam displacement, and turbulence effects. Moreover, the combined effect of using a large number of reflecting surfaces and a larger aperture diameter yields a more noticeable improvement.

Index Terms—Visible light communication (VLC), intelligent reflecting surface (IRS), underwater optical wireless communication (UOWC), Internet-of-Underwater-Things (IoUT).

I. INTRODUCTION

THE Internet-of-Underwater-Things (IoUT) is gaining increased interest as a promising concept that aims to bring ubiquitous connectivity to the underwater environment. The overarching goal of the research in this area is to connect underwater sensor networks (USNs) and autonomous

underwater vehicles (AUVs) through reliable wireless links in order to facilitate seamless underwater operations such as undersea monitoring, marine life protection, oil and gas exploration, and navigation support, to name a few [1], [2]. Communication in IoUT can be established based on three different types of propagation media, namely: acoustic, radio frequency (RF), and optical. While acoustic signals can propagate for long distances, they typically only support low data rates. RF signals, on the other hand, support higher data rates but at the expense of decreased communication range. Visible light communication (VLC), as a subset of underwater optical wireless communication (UOWC), is particularly well-suited to underwater applications as it allows sufficiently high data rates and low latency at medium transmission ranges [3].

The continuing advancements in solid-state lighting and optical detectors are paving the way for wide adoption of UOWC systems. In UOWC, the information is encoded on the intensity of the light beams emitted by light-emitting diodes (LEDs) or laser diodes (LDs) and the receiver side employs photo-detectors (PDs) to detect the fluctuations in the received light intensity and translate it into a decodable signal [4]. UOWC is a viable solution for providing low-power, low-cost, high-speed underwater communications. For example, an UOWC link utilising LDs was demonstrated in [5] offering a data rate of 1.5 Gbps over a 20 m distance. In [6], adaptive bit-power loading discrete multi-tone modulation combined with nonlinear equalisation was shown to enhance the capacity of UOWC, achieving a 7.33 Gbps over a 15 m distance. A transmission distance of 56 m was realised in [7] based on frequency domain equalisation combined with a time-domain decision feedback noise predictor at the receiver. More recently, a record transmission range of 150 m offering a data rate of 500 Mbps was demonstrated in [8] based on combination of partial response shaping, interleaving, precoding, and Trellis coded modulation technology. It is noted that one of the obstacles of achieving ubiquitous UOWC connectivity in IoUT is the limitation on the transmission range as well as the susceptibility to turbulence caused by the random variations of the refractive index of water, which leads to both intensity and phase fluctuation of the optical beams. A possible solution is to use high-sensitivity detectors which relax the alignment requirement such as photon-counting receivers [9] and avalanche diodes [10]. Nonetheless, these types of detectors are typically characterised with low modulation bandwidth compared to traditional photo-detectors, which reduces the spectral efficiency and achievable capacity.

Manuscript received 7 December 2022; revised 5 January 2023; accepted 8 January 2023. Date of publication 10 January 2023; date of current version 27 January 2023. (*Corresponding author: Yalçın Ata.*)

Yalçın Ata is with the Department of Electrical and Electronics Engineering, OSTIM Technical University, 06347 Ankara, Turkey (e-mail: ylc-nata@gmail.com).

Hanaa Abumarshoud and Muhammad Ali Imran are with the James Watt School of Engineering, University of Glasgow, Glasgow G12 8QQ, U.K. (e-mail: hanaa.abumarshoud@glasgow.ac.uk; muhammad.imran@glasgow.ac.uk).

Lina Bariah is with the Technology Innovation Institute, Abu Dhabi 9639, UAE (e-mail: lina.bariah@ieee.org).

Sami Muhaidat is with the KU Center for Cyber-Physical Systems, Department of Electrical and Computer Engineering, Khalifa University, Abu Dhabi 127788, UAE, and also with Department of Systems and Computer Engineering, Carleton University, Ottawa, ON K1S 5B6, Canada (e-mail: sami.muhammad@ku.ac.ae).

Digital Object Identifier 10.1109/JPHOT.2023.3235916

The emerging concept of intelligent reflecting surfaces (IRSs) opens the door for the possibility of controlling and optimising the wireless medium in underwater communications. IRS technology offers a change of paradigm by introducing metasurface structures that can be programmed and reconfigured to achieve a specific response to the incident signals [11]. Utilising these structures, the optical radiation can be manipulated by introducing engineered responses that affect one or more of the light wave characteristics, i.e., amplitude, phase, polarisation, spatial power distribution, and wavefront shape. Based on this, the propagation of the wireless signal can be controlled in order to achieve specific quality-of-service (QoS) requirements in terms of throughput, coverage, reliability, security, etc [12]. Moreover, the use of multiple IRSs within the UOWC network allows the possibility of creating multi-hop transmission by directing and steering the light beams, establishing non-line-of-sight (NLoS) connections between the IoUT entities [13]. However, the feasibility of this approach is mainly dependent on the characteristics and capabilities of the employed reflecting surfaces. Recently, mitigating the turbulence effect by using IRSs was investigated for Gamma distributed channel and Nikishov's power spectrum model and the associated bit-error-rate (BER) performance of the system was presented [14]. However, there is a need to evaluate the IRS effect under various underwater turbulence conditions to get a better idea of the feasibility and effectiveness of this technology.

In this paper, we investigate the outage probability performance of IRS-assisted VLC links taking into account the effects of attenuation, pointing error, and turbulence. We model the underwater turbulent medium by the recently introduced Oceanic Turbulence Optical Power Spectrum (OTOPS) model that uses practical values for the average temperature and average salinity concentration in earth basins. Our results indicate that the integration of IRSs in the underwater medium can offer significant enhancement in the link reliability under attenuation, beam displacement, and turbulence effects.

The rest of the paper is organised as follows; Section II describes the system and channel model of IRS-assisted UOWC. The outage probability derivations are shown in Section III while Section IV presents and discusses the obtained numerical results. Finally, the conclusions are drawn in Section V.

II. SYSTEM AND CHANNEL MODEL

The block diagram of the investigated system model is given in Fig. 1. An UOWC link is configured between two platforms operating in the underwater medium and an IRS is used to create an alternative path between the transmitting and receiving entities. The communication between the underwater platforms is provided by means of a VLC link. The attenuation due to absorption and scattering phenomena is taken into account through Beer-Lambert law. The horizontal and vertical beam displacements are assumed to be independently Gaussian distributed and the pointing error is modeled by Rayleigh distribution. The Lognormal distributed channel model is chosen as the probability density function (PDF) of the underwater turbulence and the recently introduced OTOPS is used to characterise the turbulence power spectrum. The signal-to-noise-ratio (SNR)

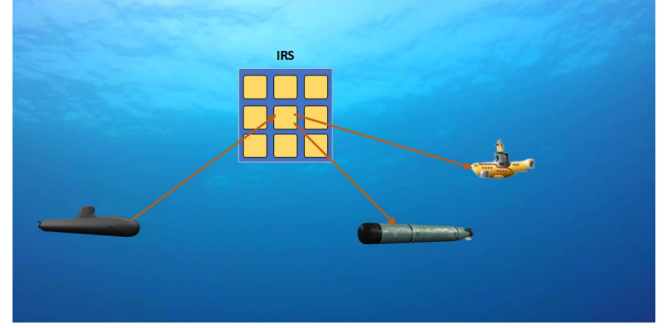


Fig. 1. System model for IRS assisted underwater VLC system.

TABLE I
WATER TYPES

Water Type	C_c in mg/m^3
Pure sea	0.005
Clear ocean	0.31
Coastal	0.83
Harbor	5.9

dependent channel PDF and cumulative distribution function (CDF) are obtained by combining the effects of attenuation, pointing error and underwater turbulence. The performance of the UOWC system is analysed in terms of outage probability.

A. Attenuation

According to the Beer-Lambert's law, the attenuation due to absorption and scattering can be expressed as

$$h_l = \exp(-c(\lambda) \cdot L), \quad (1)$$

where $c(\lambda)$ is the attenuation coefficient, λ is the wavelength and L is the link length. The attenuation coefficient $c(\lambda)$ can be written as the sum of absorption and scattering coefficients, $c(\lambda) = a(\lambda) + b(\lambda)$. Absorption remains the most dominant factor on optical beams in underwater medium and is mainly dependent on the chlorophyll concentration. The classification of waters is generally based on chlorophyll concentration, as given in Table I [15]. The absorption coefficient given in (1) is decomposed as [16], [17]

$$a(\lambda) = a_w(\lambda) + a_{cl}(\lambda) + a_f(\lambda) + a_h(\lambda), \quad (2)$$

where $a_w(\lambda)$ is the absorption coefficient of pure water (1/m) and is given for optically and chemically pure water depending on the wavelength [18], $a_{cl}(\lambda) = a_c^0(\lambda) \times (C_c/C_c^0)^{0.0602}$ is the absorption coefficient of chlorophyll, $a_c^0(\lambda)$ is the specific absorption coefficient of chlorophyll, $C_c^0 = 1 \text{ mg}/\text{m}^3$ is the chlorophyll concentration, C_c is the total concentration of the chlorophyll in mg/m^3 , $a_f(\lambda) = a_f^0 C_f \exp(-k_f \lambda)$ is the absorption coefficient of fulvic acid, $a_f^0 = 35.959 \text{ m}^2/\text{mg}$ is the specific absorption of fulvic acid, $C_f = 1.74098 \times C_c \exp[0.12327(C_c/C_c^0)]$ is the concentration of fulvic acid in mg/m^3 , $k_f = 0.0189/\text{nm}$, $a_h(\lambda) = a_h^0 C_h \exp(-k_h \lambda)$ is the absorption coefficient of humic acid, $a_h^0 = 18.828 \text{ m}^2/\text{mg}$ is the specific absorption of humic acid, $C_h = 0.19334 \times C_c \exp[0.12343(C_c/C_c^0)]$ is the concentration of humic acid in mg/m^3 , $k_h = 0.01105/\text{nm}$.

The scattering coefficient $b(\lambda)$ in (1) is given by [16], [17]

$$b(\lambda) = b_w(\lambda) + b_s^0(\lambda) \times C_s + b_l^0(\lambda) \times C_l, \quad (3)$$

where $b_w(\lambda) = 0.005826(400/\lambda)^{4.322}$ is the scattering coefficient of pure water [18], $b_s^0(\lambda) = 1.151302(400/\lambda)^{1.7}$ is the scattering due to small particles, $b_l^0(\lambda) = 0.3411(400/\lambda)^{0.3}$ is the scattering due to large particles, $C_s = 0.01739 \times C_c \exp[0.11631(C_c/C_c^0)]$ and $C_l = 0.76284 \times C_c \exp[0.03092(C_c/C_c^0)]$.

B. Pointing Error

The PDF of the pointing error is [19]

$$f_{h_p}(h_p) = \frac{\xi^2}{A_0^2 h_p^{\xi^2 - 1}}, \quad 0 \leq h_p \leq A_0 \quad (4)$$

where $\xi = \omega_{z_{eq}}/2\sigma_s$, $\omega_{z_{eq}} = \omega_z \sqrt{\frac{\pi \text{erf}(v)}{2v \exp(-v^2)}}$ is the equivalent beam radius, ω_z is the beam waist, $v = \frac{\sqrt{\pi} r_a}{\sqrt{2}\omega_z}$, $r_a = D_G/2$ is the receiver circular aperture radius, D_G is the receiver aperture diameter, σ_s is the standart deviation of pointing error, and $A_0 = [\text{erf}(v)]^2$.

C. Underwater Turbulence

The PDF of underwater turbulent channel modeled by log-normal distribution is found to be [20]

$$f_{h_a}(h_a) = \frac{1}{h_a \sqrt{2\pi\sigma_a^2}} \exp\left\{-\frac{[\ln(h_a) + \sigma_a^2/2]^2}{2\sigma_a^2}\right\}, \quad h_a > 0 \quad (5)$$

where $\sigma_a^2 = \ln(\sigma_I^2 + 1)$ is the log-amplitude variance, σ_I^2 is the scintillation index and is given for propagating Gaussian beam and apertured receiver by [20]

$$\sigma_I^2(D_G) = \exp[\sigma_{\ln X}^2(D_G) + \sigma_{\ln Y}^2(D_G)] - 1, \quad (6)$$

where $\sigma_{\ln X}^2(D_G)$ and $\sigma_{\ln Y}^2(D_G)$ denote the log variances of large-scale and small-scale, respectively and they are expressed by [20]

$$\sigma_{\ln X}^2 = \frac{0.49 \left(\frac{\Omega_G - \Lambda_1}{\Omega_G + \Lambda_1}\right)^2 \sigma_B^2}{\left[1 + \frac{0.4(2 - \bar{\Theta}_1)(\sigma_B/\sigma_r)^{12/7}}{(\Omega_G + \Lambda_1)\left(\frac{1}{3} - \frac{1}{2}\bar{\Theta}_1 + \frac{1}{3}\bar{\Theta}_1^2\right)^{6/7}} + \frac{0.56(1 + \Theta_1)}{\sigma_B^{-12/5}}\right]^{7/6}}, \quad (7)$$

$$\sigma_{\ln Y}^2 = \frac{0.51\sigma_B^2 \left(1 + 0.69\sigma_B^{12/5}\right)^{-5/6}}{1 + \left[1.20(\sigma_R/\sigma_B)^{12/5} + 0.83\sigma_R^{12/5}\right] / (\Omega_G + \Lambda_1)}. \quad (8)$$

In the previous equations, σ_R^2 is the Rytov variance of the plane wave, σ_B^2 is the Rytov variance of the Gaussian beam wave, $\Omega_G = 2L/kW_G^2$ is the parameter characterising the spot radius of the collecting lens, W_G is the radius of the Gaussian lens and $D_G^2 = 8W_G^2$, $\Lambda_1 = \Lambda_0/(\Theta_0^2 + \Lambda_0^2)$ is the Fresnel ratio of Gaussian beam at receiver, $\Lambda_0 = 2L/kW_0^2$, W_0 is the beam radius, $\Theta_0 = 1 - L/F_0$ is the beam curvature parameter at the transmitter, F_0 is the phase front radius of curvature, $\bar{\Theta}_1 =$

$1 - \Theta_1$ is the complementary parameter, $\Theta_1 = \Theta_0/(\Theta_0^2 + \Lambda_0^2)$ is the beam curvature parameter at receiver. The Rytov variances for plane and Gaussian beam waves are analytically obtained for underwater medium using OTOPS model as [21], [22]

$$\sigma_R^2 = \frac{2.9625k^{7/6}L^{11/6}\beta_0}{\varepsilon^{1/3}} (A^2\chi_T + B^2\chi_S + 2AB\chi_{TS}), \quad (9)$$

$$\sigma_B^2 = 20.9845k^{7/6}L^{11/6}\beta_0\varepsilon^{-1/3} (A^2\chi_T + B^2\chi_S + 2AB\chi_{TS}) \times \text{Re} \left[i^{5/6} \frac{6}{11} {}_2F_1 \left(\frac{-5}{6}, \frac{11}{6}; \frac{17}{6}; (\bar{\Theta}_1 + \Lambda_1 i) \right) - \frac{3}{8} \Lambda_1^{5/6} \right], \quad (10)$$

where $k = 2\pi/\lambda$ is the wave number, L is the link length, $\beta_0 = 0.72$, ε is the energy dissipation rate, χ_T is the temperature dissipation rate, $\chi_S = d_r\chi_T/H^2$ and $\chi_{TS} = 0.5(1 + d_r)\chi_T/H$ are the ensemble-averaged variance for salinity and co-spectrum dissipation rates, d_r is the eddy diffusivity ratio, H is the temperature-salinity gradient ratio, ${}_2F_1(\cdot)$ is the hypergeometric function, A and B are the linear coefficients depending on the average temperature $\langle T \rangle$, average salinity concentration $\langle S \rangle$. The eddy diffusivity ratio that is used for χ_S and χ_{TS} calculation is [23]

$$d_r = \begin{cases} R_p + R_p^{0.5}(R_p - 1)^{0.5}, & R_p \geq 1, \\ 1.85R_p - 0.85, & 0.5 \leq R_p < 1, \\ 0.15R_p, & R_p < 0.5, \end{cases} \quad (11)$$

where $R_p = |H|\alpha_T/\beta_S$ is the density ratio, α_T is the thermal expansion coefficient and β_S is the saline contraction coefficient.

The linear coefficients A and B are expressed by [24], [25]

$$A = \frac{\partial n}{\partial T} \Big|_{T=\langle T \rangle, S=\langle S \rangle}, \quad (12)$$

$$B = \frac{\partial n}{\partial S} \Big|_{T=\langle T \rangle, S=\langle S \rangle}, \quad (13)$$

where $n(T, S, \lambda)$ is the refractive index of seawater and empirically obtained as [26]

$$n(T, S, \lambda) = a_0 + (a_1 + a_2T + a_3T^2)S + a_4T^2 + (a_5 + a_6S + a_7T)\lambda^{-1} + a_8\lambda^{-2} + a_9\lambda^{-3}, \quad (14)$$

where $a_0 = 1.31405$, $a_1 = 1.779 \times 10^{-4}$, $a_2 = -1.05 \times 10^{-6}$, $a_3 = 1.6 \times 10^{-8}$, $a_4 = -2.02 \times 10^{-6}$, $a_5 = 15.868$, $a_6 = 0.01155$, $a_7 = -0.00423$, $a_8 = -4382$, $a_9 = 1.1455 \times 10^6$, T is the temperature and S is the salinity concentration. The OTOPS power spectrum is modeled by [24]

$$\Phi_n(\kappa, \langle T \rangle, \langle S \rangle, \lambda) = A^2\Phi_T + B^2\Phi_S + 2AB\Phi_{TS}, \quad (15)$$

where each spectrum is expressed by

$$\Phi_i(\kappa, \langle T \rangle, \langle S \rangle, \lambda) = \frac{1}{4\pi} \beta_0 \varepsilon^{-1/3} \kappa^{-11/3} \chi_i [1 + 21.61(\kappa\eta)^{0.61} c_i^{0.02} - 18.18(\kappa\eta)^{0.55} c_i^{0.04}] \times \exp[-174.90(\kappa\eta)^2 c_i^{0.96}]. \quad (16)$$

where η is the Kolmogorov microscale length, the non-dimensional coefficients c_i are given as $c_T = 0.072^{4/3} \beta_0 P_r^{-1}$, $c_S = 0.072^{4/3} \beta_0 S_c^{-1}$ and $c_{TS} = \frac{0.072^{4/3}}{2} \beta_0 (P_r + S_c) P_r^{-1} S_c^{-1}$ where $P_r = \mu c_p / \sigma_T$ is Prandtl number, μ is the dynamic viscosity, c_p is the specific heat, σ_T is the thermal conductivity, $S_c = \mu^2 / [5.954 \times 10^{-15} ((T) + 273.15) \rho]$ is Schmidt number and ρ is the water density. The details of the parameters and their derivations are given in [24], [25].

D. Light Propagation Model

Considering that a UOWC system using intensity modulation and direct detection scheme (IM/DD) operates in underwater medium and additive white Gaussian noise (AWGN) n_0 with zero mean and variance σ_n^2 is incorporated to the transmitted signal at the receiver.

The received signal can be written as

$$y = \sum_{n=1}^N h_{sr_n} \beta_n e^{j\theta_n} g_{ru_n} x + n_0, \quad (17)$$

where $h_{sr_n} = v_n e^{-j\phi_n}$ and $g_{ru_n} = u_n e^{-j\varphi_n}$ represent the path gain of first (source to IRS) and second (IRS to user) links, $v_n = h_{a1n} h_{p1n} h_{l1n}$ for the first link with length of L_1 and $u_n = h_{a2n} h_{p2n} h_{l2n}$ for the second link with length of L_2 including turbulence, pointing error and attenuation effects, x is transmitted signal, $\beta_n \in [0, 1]$ is the reflection amplitude of the n^{th} reflecting element, $\theta_n \in [0, 2\pi]$ is the phase shift induced by the n^{th} reflecting element, and N is the total number of reflecting elements in the IRS array.

We can write (17) in matrix form as

$$y = \mathbf{g}_{ru}^T \Theta \mathbf{h}_{sr} x + n_0, \quad (18)$$

where $\mathbf{h}_{sr} = [h_{sr_1} h_{sr_2} h_{sr_3} \dots h_{sr_N}]^T$ and $\mathbf{g}_{ru} = [g_{ru_1} g_{ru_2} g_{ru_3} \dots g_{ru_N}]^T$. Moreover, the phase shift and reflection applied by the IRS can be expressed as $\Theta = \text{diag}([\beta_1 e^{-j\theta_1} \beta_2 e^{-j\theta_2} \beta_3 e^{-j\theta_3} \dots \beta_N e^{-j\theta_N}])^T$.

Consequently, (18) can be arranged as

$$\begin{aligned} y &= \sum_{n=1}^N v_n e^{-j\phi_n} \beta_n e^{j\theta_n} u_n e^{-j\varphi_n} x + n_0 \\ &= \sum_{n=1}^N v_n \beta_n u_n e^{-j(\theta_n - \phi_n - \varphi_n)} x + n_0. \end{aligned} \quad (19)$$

We assume that the IRS reflecting elements are set such that $\theta_n = \phi_n + \varphi_n$ in order to provide the maximum SNR. Based on that, (19) can be written as

$$y = \sum_{n=1}^N v_n \beta_n u_n x + n_0. \quad (20)$$

We assume that all the IRS reflecting elements are identical having the same reflection coefficient, i.e., $\beta_n = \beta$ for $n = 1, 2, \dots, N$, then the instantaneous electrical SNR can be defined as

$$\gamma = \frac{\left(\sum_{n=1}^N v_n u_n\right)^2 \beta^2 P_t^2}{\sigma_n^2} = \frac{\left(\sum_{n=1}^N h_n\right)^2 \beta^2 P_t^2}{\sigma_n^2}, \quad (21)$$

where $h_n = v_n u_n$ since the phase has been compensated. The average SNR can be written as $\bar{\gamma} = P_t / \sigma_n^2$. The link length between transmitter and receiver can be approximated as $L \approx L_1 + L_2$. Then, assuming that random variables h_1, h_2, \dots, h_N are independent and identically distributed (i.i.d.), SNR expression becomes

$$\gamma = \bar{\gamma} N^2 \beta^2 h^2, \quad (22)$$

where h is the total channel state.

III. OUTAGE PROBABILITY ANALYSIS

The channel state including the underwater turbulence, beam displacement and attenuation effects can be written as $h = h_a h_p h_l$. Then, the PDF of the combined channel state becomes [27]

$$f_h(h) = \int f_{h|h_a}(h|h_a) f_{h_a}(h_a) dh_a, \quad (23)$$

where $f_{h|h_a}(h|h_a)$ is the conditional probability and is shown by

$$f_{h|h_a}(h|h_a) = \frac{1}{h_a h_l} f_{h_p} \left(\frac{h}{h_a h_l} \right) = \frac{\xi^2}{A_0^{\xi^2} h_a h_l} \left(\frac{h}{h_a h_l} \right)^{\xi^2 - 1}, \quad (24)$$

where $0 \leq h \leq A_0 h_a h_l$. Then, inserting (5) and (24) into (23)

$$f_h(h) = \frac{\xi^2 h^{\xi^2 - 1}}{A_0^{\xi^2} h_l^{\xi^2}} \int_{\frac{h}{A_0 h_l}}^{\infty} \frac{1}{h_a^{\xi^2}} \exp \left\{ -\frac{[\ln(h_a) + \sigma_l^2/2]^2}{2\sigma_l^2} \right\} dh_a. \quad (25)$$

Expanding the exponential term in (25) as

$$\begin{aligned} &\exp \left\{ -\frac{[\ln(h_a) + \sigma_l^2/2]^2}{2\sigma_l^2} \right\} \\ &= \exp \left[-\frac{\ln^2(h_a)}{2\sigma_l^2} \right] \exp \left[-\frac{\ln(h_a)}{2} \right] \exp \left(-\frac{\sigma_l^2}{8} \right). \end{aligned} \quad (26)$$

Then, (25) becomes

$$\begin{aligned} f_h(h) &= \frac{\xi^2 h^{\xi^2 - 1} \exp \left(-\frac{\sigma_l^2}{8} \right)}{A_0^{\xi^2} h_l^{\xi^2}} \\ &\times \int_{\frac{h}{A_0 h_l}}^{\infty} \frac{1}{h_a^{\xi^2 + 1/2}} \exp \left[-\frac{\ln^2(h_a)}{2\sigma_l^2} \right] dh_a. \end{aligned} \quad (27)$$

Changing variable as $\delta = \frac{\ln(h_a)}{\sqrt{2\sigma_l^2}}$, (27) takes the form

$$\begin{aligned} f_h(h) &= \frac{\xi^2 h^{\xi^2 - 1} \exp \left(-\frac{\sigma_l^2}{8} \right) \sqrt{2\sigma_l^2}}{A_0^{\xi^2} h_l^{\xi^2}} \\ &\times \int_{\frac{\ln(\frac{h}{A_0 h_l})}{\sqrt{2\sigma_l^2}}}^{\infty} \exp \left[-\delta^2 - (\xi^2 - 1/2) \sqrt{2\sigma_l^2} \delta \right] d\delta. \end{aligned} \quad (28)$$

To solve integral given in (28), we can use Eq. (3.322-1) of [28] that is given by

$$\int_u^\infty \exp(-x^2 - 2ax) dx = \frac{\sqrt{\pi}e^{a^2}}{2} [1 - \operatorname{erf}(u + a)]. \quad (29)$$

Applying (29) to (28), we arrive

$$f_h(h) = \frac{\xi^2 h^{\xi^2-1} \exp\left(-\frac{\sigma_l^2}{8}\right) \sqrt{2\pi\sigma_l^2}}{2A_0^{\xi^2} h_l^{\xi^2}} \exp\left[\frac{(\xi^2 - 1/2)^2 \sigma_l^2}{2}\right] \times \left\{ 1 - \operatorname{erf}\left[\frac{(\xi^2 - 1/2)\sqrt{2\sigma_l^2}}{2} + \frac{1}{\sqrt{2\sigma_l^2}} \ln\left(\frac{h}{A_0 h_l}\right)\right] \right\}. \quad (30)$$

In (30), obtained PDF depends on the combined channel state h including the attenuation, turbulence and pointing effects. We also note that the channel state h is only for one source to user link. Since we are assuming that the random variables h_1, h_2, \dots, h_N are independent and identically distributed ($h_1 = h_2 = \dots = h_N = h$), the PDF of the instantaneous SNR including all links through each IRS surface can be expressed depending on the average SNR and number of used IRS surfaces. Similar approximation is used in [14]. Using the transformation given in [14], [29], the PDF of SNR for lognormal distribution can be written as

$$f_\gamma(\gamma) = f_h\left(\sqrt{\frac{\gamma}{\bar{\gamma}N^2\beta^2}}\right) \left|\frac{dh}{d\gamma}\right|. \quad (31)$$

Using the relationships given in (22) and (31), the SNR dependent PDF can be obtained as

$$f_\gamma(\gamma) = \frac{\gamma^{\xi^2/2-1} \xi^2 \exp\left(-\frac{\sigma_l^2}{8}\right) \sqrt{2\pi\sigma_l^2}}{4A_0^{\xi^2} h_l^{\xi^2} (\sqrt{\bar{\gamma}N^2\beta^2})^{\xi^2}} \exp\left[\frac{(\xi^2 - 1/2)^2 \sigma_l^2}{2}\right] \times \left\{ 1 - \operatorname{erf}\left[\frac{(\xi^2 - 1/2)\sqrt{2\sigma_l^2}}{2} + \frac{1}{2\sqrt{2\sigma_l^2}} \ln\left(\frac{\gamma}{\bar{\gamma}N^2\beta^2 A_0^2 h_l^2}\right)\right] \right\}. \quad (32)$$

The CDF of SNR γ is found by

$$F_\gamma(\gamma) = \int_0^\gamma f_\gamma(x) dx. \quad (33)$$

Inserting (32) into (33), we have

$$F_\gamma(\gamma) = \frac{\xi^2 \exp\left(-\frac{\sigma_l^2}{8}\right) \sqrt{2\pi\sigma_l^2}}{4A_0^{\xi^2} h_l^{\xi^2} (\sqrt{\bar{\gamma}N^2\beta^2})^{\xi^2}} \exp\left[\frac{(\xi^2 - 1/2)^2 \sigma_l^2}{2}\right] \times \int_0^\gamma x^{\xi^2/2-1} \left\{ 1 - \operatorname{erf}\left[\frac{(\xi^2 - 1/2)\sqrt{2\sigma_l^2}}{2} + \frac{1}{2\sqrt{2\sigma_l^2}} \ln\left(\frac{x}{\bar{\gamma}N^2\beta^2 A_0^2 h_l^2}\right)\right] \right\} dx. \quad (34)$$

There are two integral parts in (34). The first part can be taken as $\int_0^\gamma x^{\xi^2/2-1} dx = \frac{2\gamma^{\xi^2/2}}{\xi^2}$. The second integration

is challenging and changing parameters as $\frac{(\xi^2-1/2)\sqrt{2\sigma_l^2}}{2} + \frac{1}{2\sqrt{2\sigma_l^2}} \ln\left(\frac{x}{\bar{\gamma}N^2\beta^2 A_0^2 h_l^2}\right) = t$ will result in a new equation as

$$F_\gamma(\gamma) = \frac{\xi^2 \exp\left(-\frac{\sigma_l^2}{8}\right) \sqrt{2\pi\sigma_l^2}}{4A_0^{\xi^2} h_l^{\xi^2} (\sqrt{\bar{\gamma}N^2\beta^2})^{\xi^2}} \exp\left[\frac{(\xi^2 - 1/2)^2 \sigma_l^2}{2}\right] \times \left\{ \frac{2\gamma^{\xi^2/2}}{\xi^2} - 2\sqrt{2\sigma_l^2} (\bar{\gamma}N^2\beta^2 A_0^2 h_l^2)^{\xi^2/2} \times \exp[-2\sigma_l^2(\xi^2/2)(\xi^2 - 1/2)] \times \int_{-\infty}^{\Delta_1} \exp\left[2\sqrt{2\sigma_l^2}(\xi^2/2)t\right] \operatorname{erf}(t) dt \right\}, \quad (35)$$

where $\Delta_1 = \frac{(\xi^2-1/2)\sqrt{2\sigma_l^2}}{2} + \frac{1}{2\sqrt{2\sigma_l^2}} \ln\left(\frac{\gamma}{\bar{\gamma}N^2\beta^2 A_0^2 h_l^2}\right)$. Dividing integration in (35) and using some mathematical manipulations and the odd function property of erf, (35) turns into two-parts integral as

$$F_\gamma(\gamma) = \frac{\xi^2 \exp\left(-\frac{\sigma_l^2}{8}\right) \sqrt{2\pi\sigma_l^2}}{4A_0^{\xi^2} h_l^{\xi^2} (\sqrt{\bar{\gamma}N^2\beta^2})^{\xi^2}} \exp\left[\frac{(\xi^2 - 1/2)^2 \sigma_l^2}{2}\right] \times \left(\frac{2\gamma^{\xi^2/2}}{\xi^2} - 2\sqrt{2\sigma_l^2} (\bar{\gamma}N^2\beta^2 A_0^2 h_l^2)^{\xi^2/2} \times \exp[-2\sigma_l^2(\xi^2/2)(\xi^2 - 1/2)] \times \left\{ -\int_0^\infty \exp\left[-\sqrt{2\sigma_l^2}\xi^2 u\right] \operatorname{erf}(u) du + \int_0^{\Delta_1} \exp\left[\sqrt{2\sigma_l^2}\xi^2 t\right] \operatorname{erf}(t) dt \right\} \right). \quad (36)$$

It is seen that the u dependent integral in (36) is in the Laplace transform structure that is expressed by $\mathcal{L}\{f(t)\}(s) = \int_0^\infty f(t)e^{-st} dt$. The Laplace transform of erf is given as [30]

$$\mathcal{L}\{\operatorname{erf}(t)\}(s) = \frac{1}{s} \exp(s^2/4) \operatorname{erfc}(s/2), \operatorname{Re}(s) > 0. \quad (37)$$

The second part integration can be solved by using following equation that is given by [31]

$$\int_0^b \exp(at) \operatorname{erf}(t) dt = \frac{1}{a} \left\{ \exp(a^2/4) [\operatorname{erf}(a/2 - b) - \operatorname{erf}(a/2)] + \exp(ab) \operatorname{erf}(b) \right\}. \quad (38)$$

Applying (37) and (38) to (36), the CDF of underwater turbulent medium including the effects of attenuation, pointing error and turbulence can be found as

$$F_\gamma(\gamma) = \frac{\exp\left(-\frac{\sigma_l^2}{8}\right) \sqrt{2\pi\sigma_l^2}}{2A_0^{\xi^2} h_l^{\xi^2} (\sqrt{\bar{\gamma}N^2\beta^2})^{\xi^2}} \exp\left[\frac{(\xi^2 - 1/2)^2 \sigma_l^2}{2}\right] \times \left[\gamma^{\xi^2/2} - (\bar{\gamma}N^2\beta^2 A_0^2 h_l^2)^{\xi^2/2} \exp[-\sigma_l^2 \xi^2 (\xi^2 - 1/2)] \right]$$

$$\begin{aligned}
& \times \left(-\exp\left(\frac{\sigma_l^2 \xi^4}{2}\right) \operatorname{erfc}\left(\frac{\sqrt{2\sigma_l^2 \xi^2}}{2}\right) + \exp\left(\frac{\sigma_l^2 \xi^4}{2}\right) \right. \\
& \times \left\{ \operatorname{erf}\left[\frac{\sqrt{2\sigma_l^2}}{4} - \frac{1}{2\sqrt{2\sigma_l^2}} \ln\left(\frac{\gamma}{\bar{\gamma} N^2 \beta^2 A_0^2 h_l^2}\right)\right] \right. \\
& \left. \left. - \operatorname{erf}\left(\frac{\sqrt{2\sigma_l^2 \xi^2}}{2}\right) \right\} + \exp\left[\sigma_l^2 \xi^2 (\xi^2 - 1/2) + \frac{\xi^2}{2}\right] \right. \\
& \times \ln\left(\frac{\gamma}{\bar{\gamma} N^2 \beta^2 A_0^2 h_l^2}\right) \left. \operatorname{erf}\left[\frac{(\xi^2 - 1/2)\sqrt{2\sigma_l^2}}{2}\right] \right. \\
& \left. \left. + \frac{1}{2\sqrt{2\sigma_l^2}} \ln\left(\frac{\gamma}{\bar{\gamma} N^2 \beta^2 A_0^2 h_l^2}\right) \right] \right]. \quad (39)
\end{aligned}$$

The outage probability of VLC system operating in underwater medium, which can be defined the probability of instantaneous SNR γ falls below the defined threshold SNR level γ_{th} , can be found by

$$P_{out} = P_r(\gamma \leq \gamma_{th}) = F_\gamma(\gamma_{th}). \quad (40)$$

Then, the outage probability will be obtained as

$$\begin{aligned}
P_{out} &= \frac{\exp\left(-\frac{\sigma_l^2}{8}\right) \sqrt{2\pi\sigma_l^2}}{2A_0^2 h_l^2 \xi^2 \left(\sqrt{\bar{\gamma} N^2 \beta^2}\right)^{\xi^2}} \exp\left[\frac{(\xi^2 - 1/2)^2 \sigma_l^2}{2}\right] \\
& \times \left[\gamma_{th}^{\xi^2/2} - (\bar{\gamma} N^2 \beta^2 A_0^2 h_l^2)^{\xi^2/2} \exp\left[-\sigma_l^2 \xi^2 (\xi^2 - 1/2)\right] \right] \\
& \times \left(-\exp\left(\frac{\sigma_l^2 \xi^4}{2}\right) \operatorname{erfc}\left(\frac{\sqrt{2\sigma_l^2 \xi^2}}{2}\right) + \exp\left(\frac{\sigma_l^2 \xi^4}{2}\right) \right. \\
& \times \left\{ \operatorname{erf}\left[\frac{\sqrt{2\sigma_l^2}}{4} - \frac{1}{2\sqrt{2\sigma_l^2}} \ln\left(\frac{\gamma_{th}}{\bar{\gamma} N^2 \beta^2 A_0^2 h_l^2}\right)\right] \right. \\
& \left. \left. - \operatorname{erf}\left(\frac{\sqrt{2\sigma_l^2 \xi^2}}{2}\right) \right\} + \exp\left[\sigma_l^2 \xi^2 (\xi^2 - 1/2) + \frac{\xi^2}{2}\right] \right. \\
& \times \ln\left(\frac{\gamma_{th}}{\bar{\gamma} N^2 \beta^2 A_0^2 h_l^2}\right) \left. \operatorname{erf}\left[\frac{(\xi^2 - 1/2)\sqrt{2\sigma_l^2}}{2}\right] \right. \\
& \left. \left. + \frac{1}{2\sqrt{2\sigma_l^2}} \ln\left(\frac{\gamma_{th}}{\bar{\gamma} N^2 \beta^2 A_0^2 h_l^2}\right) \right] \right]. \quad (41)
\end{aligned}$$

IV. SIMULATION RESULTS

This section presents the outage probability variation of an IRS-assisted UOWC system using a function of various parameters in the underwater medium. Unless specified in the figures' captions or on the plots, parameters are fixed as given in Table II. It is known that the most dominant factor in underwater turbulent medium is the absorption phenomenon. The blue region of the visible light spectrum $\sim \lambda = 450 - 485$ nm provides minimum attenuation in terms of the absorption effect. In order to observe other effects besides absorption, the wavelength is chosen as $\lambda = 450$ nm. The average temperature and average salinity concentration of underwater medium are fixed to their moderate

TABLE II
FIXED PARAMETERS

Symbol	Value
λ	450 nm
$\langle T \rangle$	15 °C
$\langle S \rangle$	20 ppt
ε	$10^{-5} \text{ m}^2 \text{ s}^{-3}$
χ_T	$10^{-7} \text{ K}^2 \text{ s}^{-1}$
H	$-2^\circ \text{ ppt}^{-1}$
D_G	2 cm
W_0	2 cm
F_0	∞
γ_{th}	2 dB
$\bar{\gamma}$	40 dB
N	50
β	1
C_c	0.03 g/m^3
σ_s	$3 \times r_a$
L	20 m

levels as $\langle T \rangle = 15$ °C and $\langle S \rangle = 20$ ppt. The optical wave is the collimated Gaussian beam with $F_0 = \infty$ phase front radius of curvature and $W_0 = 2$ cm radius. The link length in underwater medium remains in the range of several tens of meters here, it is set to $L = 20$ m that is challenging but realistic for UOWC systems due to combined effects of different phenomena such as absorption, scattering, turbulence and pointing error. In underwater medium, the temperature dissipation rate χ_T and the energy dissipation rate ε change in the range of $\chi_T = 10^{-4} - 10^{-10} \text{ K}^2 \text{ s}^{-1}$ and $\varepsilon = 10^{-2} - 10^{-10} \text{ m}^2 \text{ s}^{-3}$, respectively. The values of χ_T and ε are selected for their moderate levels as $\chi_T = 10^{-7} \text{ K}^2 \text{ s}^{-1}$ and $\varepsilon = 10^{-5} \text{ m}^2 \text{ s}^{-3}$ to see the improvement better with the IRS application.

Results are obtained by using MATLAB simulation environment. To verify the accuracy of our derivations, we compared our derivations with their initial counterparts for all steps. We first validated our derivations for PDF $f_h(h)$ by comparing initial equation (25) with the PDF derivation given in (30). We performed an additional validation for our derivations by comparing the initial equation of CDF $F_\gamma(\gamma)$ given in (34) with the analytical derivation of CDF given in (39). In both cases, it was observed that initial and derived equations match perfectly which indicates the accuracy of our results.

Fig. 2 depicts the average outage probability variation depending on both the link length and the receiver aperture diameter. It can be seen that the outage probability increases with the increase in link length. Using an aperture with $D_G = 2$ cm and $N = 50$ IRS reflecting elements, the outage probability takes the values of $\sim 2.4 \times 10^{-5}$, $\sim 1.6 \times 10^{-4}$, $\sim 7.1 \times 10^{-4}$ and $\sim 2.6 \times 10^{-3}$ for the link length values of $L = 10$ m, $L = 20$ m, $L = 30$ m and, $L = 40$ m, respectively. Since we focus on the combined effect of absorption, scattering, pointing error and turbulence in this study, results show that the practical effective distance of an UOWC system operating in an underwater medium remains in a few ten meters. The increasing trend of outage probability with the link length is also seen from Fig. 3.

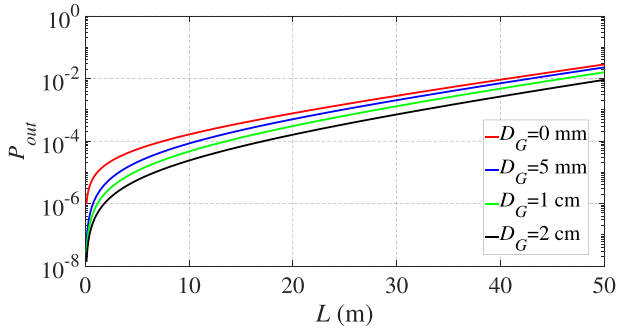


Fig. 2. Outage probability versus link length for various values of aperture diameters.

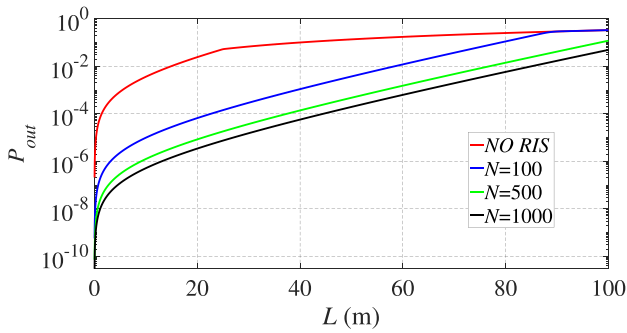


Fig. 3. Outage probability versus link length for different number of IRS surfaces.

Another conclusion from Fig. 2 is the significant reduction in outage probability with the receiver aperture averaging. For example, keeping the link length as $L = 10$ m and $N = 50$ IRS surfaces, outage probability falls from $\sim 1.6 \times 10^{-4}$ to $\sim 2.4 \times 10^{-5}$ changing the point receiver ($D_G = 0$) with the $D_G = 2$ cm apertured receiver. In Fig. 3, the benefit of using IRS for UOWC in underwater turbulent medium is observed. When link length is fixed as $L = 20$ m, outage probability takes the value of $\sim 2.4 \times 10^{-2}$ when no IRS element is used. However, outage probability maintains its reduction with the values of $\sim 6.5 \times 10^{-5}$, $\sim 8.3 \times 10^{-6}$, and $\sim 3.4 \times 10^{-6}$ with an increase in the number of IRS sequentially as $N = 100$, $N = 500$, and $N = 1000$. Changing the number of IRS from $N = 0$ up to $N = 1000$ reduces outage probability from order of 10^{-2} to the order of $(10^{-7} - 10^{-3})$ depending on the link distance. These results indicate that IRSs can provide a substantial improvement in the performance of the UOWC system. Another conclusion from Fig. 3 that using IRS may not yield benefit after a certain distance because the combined effect of attenuation, pointing error and turbulence becomes severe and outage probability values of IRS cases gradually merge to no IRS case depending on the number of IRS elements (This can be seen for $N = 100$ IRS in Fig. 3).

In Fig. 4, the outage performance of an UOWC system versus the number of IRS is plotted for various values of receiver aperture diameter. A monotonic decrease in outage probability with the increase in the number of IRS is seen. Using a receiver with $D_G = 1$ cm aperture diameter, the average BER takes the values of $\sim 7 \times 10^{-3}$ for no IRS is used. However, outage probability decreases to $\sim 1.5 \times 10^{-4}$, $\sim 1.9 \times 10^{-5}$, $\sim 2.4 \times 10^{-6}$, and

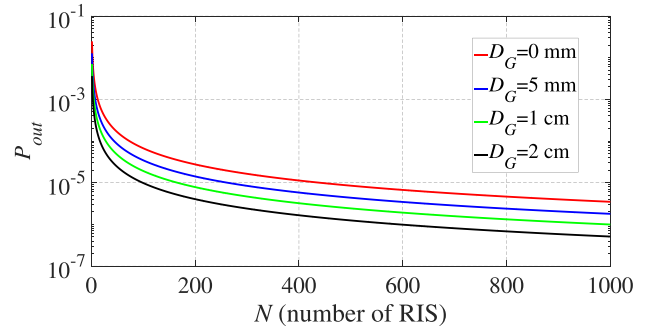


Fig. 4. Outage probability versus number of IRS surfaces for different values aperture diameters.

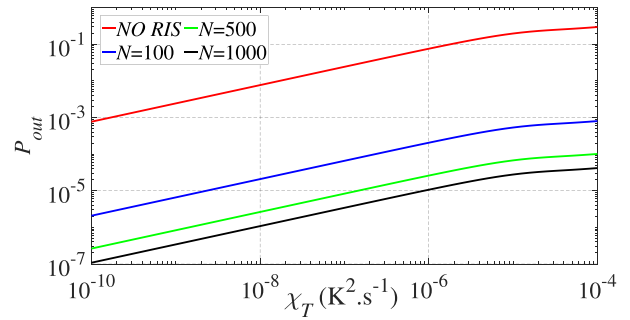


Fig. 5. Outage probability versus temperature dissipation range for various number of IRS surfaces.

$\sim 9.9 \times 10^{-7}$ when the number of IRS surfaces are increased to $N = 20$, $N = 100$, $N = 500$, and $N = 1000$, respectively. A sharp improvement in the outage performance of an UOWC system up to a certain number of IRS surface (e.g., $N \sim 200$) is seen then, outage probability decreases slower with the increase of a number of IRS surfaces. The larger the receiver aperture diameter the smaller the outage probability trend is also seen from Fig. 4. We note that the combined effect of using large number IRS and a larger aperture diameter yields more performance improvement. For example, the outage probability reaches the value of $\sim 6.7 \times 10^{-5}$ from $\sim 2.4 \times 10^{-2}$ by using $N = 100$ IRS elements for an UOWC system using a point receiver ($D_G = 0$). However, outage probability decreases to $\sim 9.8 \times 10^{-6}$ when receiver aperture diameter is increased to $D_G = 2$ cm and the number of IRS is still $N = 100$.

Fig. 5 presents the outage probability variation with the temperature dissipation rate for various numbers of IRS. One can see from Fig. 5 that the outage probability stands smaller with the smaller values of temperature dissipation rate showing the weaker turbulent power spectrum strength and hence, less turbulence effect. Keeping the number of IRS as $N = 100$, the outage probability jumps from $\sim 2.1 \times 10^{-6}$ to $\sim 8 \times 10^{-4}$ when temperature dissipation rate raises from $\chi_T = 10^{-10} \text{ K}^2\text{s}^{-1}$ to $\chi_T = 10^{-4} \text{ K}^2\text{s}^{-1}$. By observing the outage probability reduction from $\sim 7.6 \times 10^{-3}$ to $\sim 1.1 \times 10^{-6}$ with the increase of the number of IRS from $N = 0$ to $N = 1000$ for the fixed value of $\chi_T = 1 \times 10^{-8} \text{ K}^2\text{s}^{-1}$, the advantage of using IRS as a mitigation technique is obvious from Fig. 5. The effect of another dissipation rate, kinetic energy dissipation rate ϵ , is illustrated in Fig. 6. We observe that an increase in the kinetic

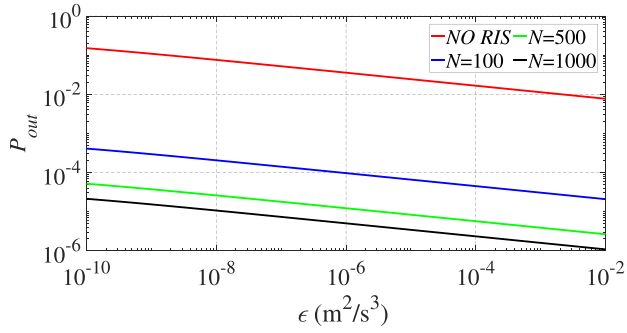


Fig. 6. Outage probability versus energy dissipation range for various number of IRS surfaces.

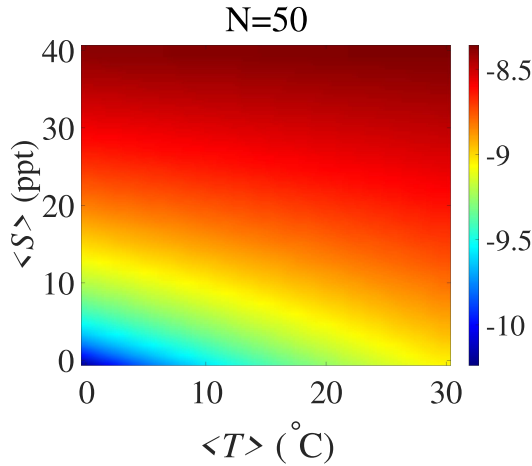


Fig. 7. Density plot of outage probability $-\log(P_{out})$ variation as functions of average temperature and average salinity concentration.

energy dissipation rate causes a fall in the outage probability showing that the performance of UOWC system improves when the underwater turbulent medium is more energetic. This can be verified by varying of outage probability from $\sim 4 \times 10^{-4}$ to $\sim 2.1 \times 10^{-5}$ with the change of kinetic energy dissipation rate from $\epsilon = 10^{-10} \text{ m}^2\text{s}^{-3}$ to $\epsilon = 10^{-2} \text{ m}^2\text{s}^{-3}$ keeping the number of IRS fixed as $N = 100$. Similar to the previous figures as a function of the number of IRS, the considerable reduction in the outage probability is also seen with the increase in the number of IRS in Fig. 6.

The $\log(P_{out})$ variation of an UOWC depending on the average temperature $\langle T \rangle$ and average salinity concentration $\langle S \rangle$ as density plots in Fig. 7. From Fig. 7, it is seen that increase in both the average temperature (horizontal axes) and the average salinity concentration (vertical axes) cause a performance degradation up to a certain level. The outage probability value has an order of magnitude around $\sim 10^{-8}$ for the number of IRS $N = 50$ when average temperature and average salinity concentration take their highest values then, outage probability decreases around $\sim 10^{-10}$ when both parameters take their lowest values.

The reflection amplitude of IRS is generally assumed to be $\beta = 1$ (perfect reflector) for the sake of simplicity in almost all studies. However, the reflection amplitude is one of the most important factors that define the efficiency of the IRS implementation. For this purpose, Fig. 8 represents the outage

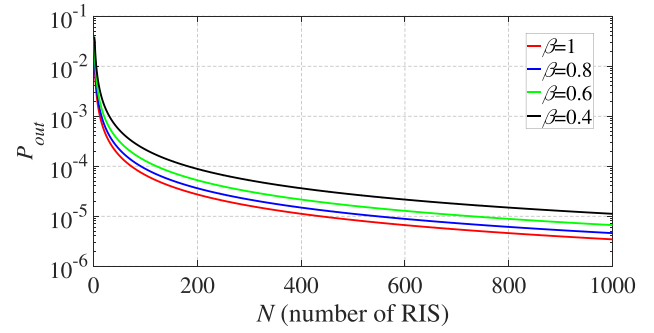


Fig. 8. Outage probability versus number of IRS surfaces for different values of reflection coefficients.

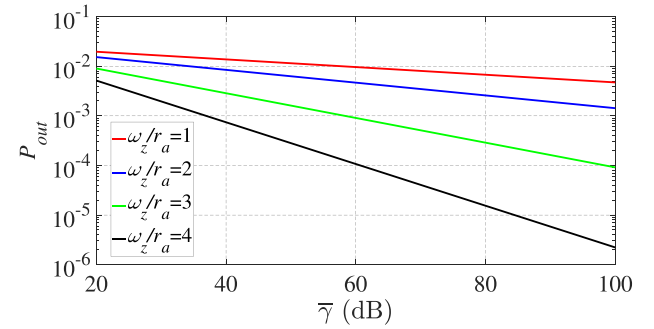


Fig. 9. Outage probability versus average SNR for different values of beam waist ($N = 40$).

probability variation versus the number of IRS for various values of reflection amplitude of IRS. It is observed from Fig. 8 that the reflection amplitude becomes a performance improving factor and outage probability remains at lower levels when reflection coefficient approximates the value of $\beta = 1$.

In Fig. 9, the outage performance of an UOWC system is illustrated as function of average SNR for various values of beam waist. The significant performance improvement effect with the average SNR increase is observed. Keeping beam waist as $\omega_b = 2 \times r_a$, the outage probability drops from $\sim 1.5 \times 10^{-2}$ to $\sim 1.4 \times 10^{-3}$ when average SNR increases from $\bar{\gamma} = 20 \text{ dB}$ to $\bar{\gamma} = 100 \text{ dB}$. It is also seen from Fig. 9 that an UOWC can benefit from the higher beam waist due to increased probability of collecting more of optical beam at the receiver aperture. While average SNR is $\bar{\gamma} = 40 \text{ dB}$, outage probability varies positively from $\sim 1.3 \times 10^{-2}$ to $\sim 7.4 \times 10^{-4}$ with the increase of beam waist from $\omega_b = 1 \times r_a$ to $\omega_b = 4 \times r_a$.

Finally, the outage performance of an UOWC system is shown for different types of waters in Fig. 10. Since waters are classified based on chlorophyll concentration, the drastic effect of chlorophyll concentration is seen. Although $N = 50$ number of IRS elements are used, the outage probability can drop below $\sim 10^{-6}$ level for average SNR values of $\bar{\gamma} = 60 \text{ dB}$, $\bar{\gamma} = 69 \text{ dB}$, and $\bar{\gamma} = 84 \text{ dB}$ in pure, clear ocean and coastal waters, respectively. However, it is not possible to catch the outage probability below $\sim 10^{-6}$ level in harbor water. These results show that underwater medium is still challenging for UOWC system and optimum distance remains as few ten meters even IRS is implemented.

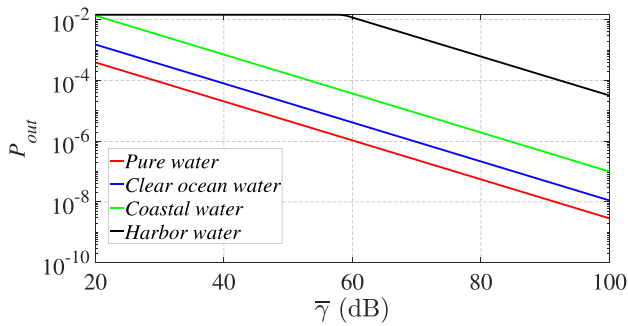


Fig. 10. Outage probability versus average SNR for different water types ($L = 10$ m).

V. CONCLUSION

The outage performance of a VLC-based UOWC system operating in an underwater turbulent medium and the effect of IRS implementation are theoretically analysed. The closed-form expression of outage probability including the IRS effect is obtained. Results show that the reliability enhancement offered by IRSs is undeniable. Using a sufficiently large number of IRS can cause a significant enhancement in the system performance. The reflection amplitude of the used IRS also remains an important factor in the outage probability performance of UOWC system. The outage probability tends to increase with the increase of link length, temperature dissipation rate, average temperature, and average salinity concentration. However, the outage probability starts to decrease with the increase of receiver aperture diameter, the number of IRS, the reflection amplitude of IRS, the kinetic energy dissipation rate and the average SNR. All these parameters need to be taken into consideration when designing and optimising IRS-assisted UOWC systems. Based on that, an optimal configuration of the number and reflection coefficients can be achieved.

REFERENCES

- [1] M. Jouhari, K. Ibrahim, H. Tembini, and J. Ben-Othman, "Underwater wireless sensor networks: A survey on enabling technologies, localization protocols, and Internet of Underwater Things," *IEEE Access*, vol. 7, pp. 96879–96899, 2019.
- [2] Mari Carmen Domingo, "An overview of the Internet of Underwater Things," *J. Netw. Comput. Appl.*, vol. 35, no. 6, pp. 1879–1890, 2012.
- [3] H. Haas, M. S. Islam, C. Chen, and H. Abumarshoud, *An Introduction to Optical Wireless Mobile Communication*. Norwood, MA, USA: Artech House, 2021.
- [4] H. Haas, E. Sarbazi, H. Marshoud, and J. Fakidis, "Visible-light communications and light fidelity," in *Optical Fiber Telecommunications VII*. New York, NY, USA: Academic Press, 2020, ch. 11, pp. 443–493.
- [5] C. Shen et al., "20-meter underwater wireless optical communication link with 1.5 Gbps data rate," *Opt. Exp.*, vol. 24, no. 22, pp. 25502–25509, Oct. 2016.
- [6] C. Fei, J. Zhang, G. Zhang, Y. Wu, X. Hong, and S. He, "Demonstration of 15-m 7.33-Gb/s 450-nm underwater wireless optical discrete multi-tone transmission using post nonlinear equalization," *J. Lightw. Technol.*, vol. 36, no. 3, pp. 728–734, Feb. 2018.
- [7] X. Chen, W. Lyu, Z. Zhang, J. Zhao, and J. Xu, "56-m/3.31-Gbps underwater wireless optical communication employing nyquist single carrier frequency domain equalization with noise prediction," *Opt. Exp.*, vol. 28, no. 16, pp. 23784–23795, Aug. 2020.

- [8] X. Chen et al., "150 m/500 Mbps underwater wireless optical communication enabled by sensitive detection and the combination of receiver-side partial response shaping and TCM technology," *J. Lightw. Technol.*, vol. 39, no. 14, pp. 4614–4621, Jul. 2021.
- [9] S. Hu, L. Mi, T. Zhou, and W. Chen, "35.88 attenuation lengths and 3.32 bits/photon underwater optical wireless communication based on photon-counting receiver with 256-PPM," *Opt. Exp.*, vol. 26, no. 17, pp. 21685–21699, Aug. 2018.
- [10] H. Chen et al., "Toward long-distance underwater wireless optical communication based on a high-sensitivity single photon avalanche diode," *IEEE Photon. J.*, vol. 12, no. 3, pp. 1–10, Jun. 2020, Art. no. 7902510.
- [11] H. Abumarshoud, L. Mohjazi, O. A. Dobre, M. D. Renzo, M. A. Imran, and H. Haas, "LiFi through reconfigurable intelligent surfaces: A new frontier for 6G?," *IEEE Veh. Technol. Mag.*, 17, no. 1, pp. 37–46, Mar. 2022.
- [12] H. Abumarshoud, B. Selim, M. Tatipamula, and H. Haas, "Intelligent reflecting surfaces for enhanced NOMA-based visible light communications," in *Proc. IEEE Int. Conf. Commun.*, 2022, pp. 571–576.
- [13] A. M. Abdelhady, O. Amin, M.-S. Alouini, and B. Shihada, "Revolutionizing optical wireless communications via smart optics," *IEEE Open J. Commun. Soc.*, vol. 3, pp. 654–669, 2022.
- [14] R. P. Naik and W.-Y. Chung, "Evaluation of reconfigurable intelligent surface-assisted underwater wireless optical communication system," *J. Lightw. Technol.*, vol. 40, no. 13, pp. 4257–4267, Jul. 2022.
- [15] C. Gabriel, M.-A. Khalighi, S. Bourennane, P. Leon, and V. Rigaud, "Channel modeling for underwater optical communication," in *Proc. IEEE GLOBECOM Workshops 2011*, pp. 833–837.
- [16] M. A. Chancey, "Short range underwater optical communication links," M.S. Thesis, North Carolina State University, Raleigh, NC, USA, 2005.
- [17] F. D. Kashani, M. R. H. Rad, and E. Kazemian, "Analyzing the propagation behavior of a Gaussian laser beam through seawater and comparing with atmosphere," *Iranian J. Elect. Electron. Eng.*, vol. 9, no. 4, pp. 197–203, 2013.
- [18] A. Morel and L. Prieur, "Analysis of variations in ocean color 1," *Limnol. Oceanogr.*, vol. 22, no. 4, pp. 709–722, 1977.
- [19] A. A. Farid and S. Hranilovic, "Outage capacity optimization for free-space optical links with pointing errors," *J. Lightw. Technol.*, vol. 25, no. 7, pp. 1702–1710, Jul. 2007.
- [20] C. L. Andrews and R. L. Phillips, *Laser Beam Propagation Through Random Media*. Breda, The Netherlands: SPIE, 2005.
- [21] Y. Ata, "Rytov variance of plane and spherical waves, and scintillation index in weak to strong underwater turbulence," *J. Opt.*, vol. 24, 2022, Art. no. 115601.
- [22] Y. Ata and K. Kiasaleh, "Analysis of optical wireless communication links in turbulent underwater channels with wide range of water parameters," *IEEE Trans. Veh. Technol.*, 2023, doi: 10.1109/TVT.2023.3235823.
- [23] M. Elamassie, M. Uysal, Y. Baykal, M. Abdallah, and K. Qaraqe, "Effect of eddy diffusivity ratio on underwater optical scintillation index," *J. Opt. Soc. Amer. A*, vol. 34, no. 11, pp. 1969–1973, 2017.
- [24] J. Yao, M. Elamassie, and O. Korotkova, "Spatial power spectrum of natural water turbulence with any average temperature, salinity concentration, and light wavelength," *J. Opt. Soc. Amer. A*, vol. 37, no. 10, pp. 1614–1621, 2020.
- [25] Y. Ata, J. Yao, and O. Korotkova, "BER variation of an optical wireless communication system in underwater turbulent medium with any temperature and salinity concentration," *Opt. Commun.*, vol. 485, 2021, Art. no. 126751.
- [26] X. Quan and E. S. Fry, "Empirical equation for the index of refraction of seawater," *Appl. Opt.*, vol. 34, no. 18, pp. 3477–3480, 1995.
- [27] H. G. Theodoros, T. A. Tsiftsis, and G. K. Karagiannidis, "Optical wireless communications with heterodyne detection over turbulence channels with pointing errors," *J. Lightw. Technol.*, vol. 27, no. 20, pp. 4440–4445, Oct. 2009.
- [28] I. S. Gradshteyn and I. M. Ryzhik, *Table of Integrals, Series, and Products*. 8th Ed., London, U.K.: Elsevier, 2014, p. 339.
- [29] Donald G. Watts, "Transformations made transparently easy, or, so that's what a Jacobian is!," *Amer. Statistician*, vol. 27, no. 1, pp. 22–25, 1973.
- [30] Wolfram Inc., "The Wolfram functions site, 2022," Accessed: Sep. 28, 2022. [Online]. Available: <https://functions.wolfram.com>
- [31] Wolfram Inc., "Wolfram alpha," Accessed: Sep. 28, 2022. [Online]. Available: <https://www.wolframalpha.com>